Journal of Power Sources 450 (2020) 227618

Contents lists available at ScienceDirect

Journal of Power Sources

journal homepage: www.elsevier.com/locate/jpowsour

Synthesis of graphene-siloxene nanosheet based layered composite materials by tuning its interface chemistry: An efficient anode with overwhelming electrochemical performances for lithium-ion batteries

K. Thileep Kumar [a,1], M. Jeevan Kumar Reddy [c,1], G. Sivagaami Sundari [a], S. Raghu [a,b], R. A. Kalaivani [a], Sung Hun Ryu [d], A.M. Shanmugharaj [a,b,*]

[a] Department of Chemistry, Vels Institute of Science, Technology and Advanced Studies (VISTAS), Chennai, 117, India
[b] Centre for Advanced Research and Development (CARD), Vels Institute of Science, Technology and Advanced Studies (VISTAS), Chennai, 117, India
[c] Department of Nanoscience and Engineering, Inje University, Republic of Korea
[d] Department of Chemical Engineering, Kyung Hee University, Yongin, Republic of Korea

HIGHLIGHTS

- A method of preparing 3D structured graphene-siloxene (SiG) composites is reported.
- Intercalation of siloxene in the graphene layers is revealed using FE-SEM and TEM.
- Prepared SiG render first charge capacity of 3016 $mAhg^{-1}$ at 205 mAg^{-1} current rate.
- At 4.1 Ag^{-1}, SiG anode delivers reversible capacity of 1040 $mAhg^{-1}$ for 1000 cycles.

GRAPHICAL ABSTRACT

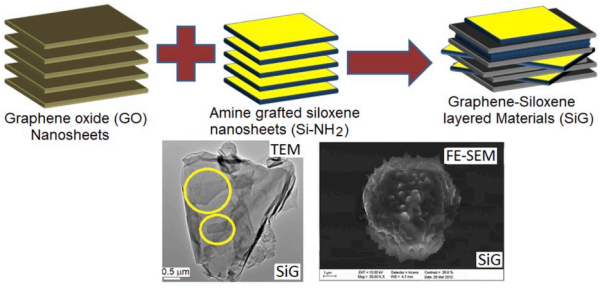

ARTICLE INFO

Keywords:
Topochemical reaction
Hydrosilylation reaction
Silicon nano sheets
Silicon-graphene
Specific capacity
Li-ion battery

ABSTRACT

Owing to its high theoretical storage capacity, two dimensional (2D) silicon nanosheets is the one among the most exciting anode material for the next generation lithium ion (Li-ion) batteries. However, deprived electrochemical properties due to the huge volume expansion resulting in rapid capacity decay, thereby hindering its commercial application aspect of silicon nanosheet based materials. The present work proposes a novel concept of synthesizing graphene-siloxene (SiG) based multi-layered structures by tuning the interface chemistries of graphene oxide and siloxene sheets derived from topochemical transformation of calcium silicide ($CaSi_2$). Morphological characterization using Field emission scanning electron microscopic and transmission electron microscopy reveal the successful formation of few- to multi-layered SiG composite materials with intercalated/surface grafted siloxene nanosheets on the graphene layers. Owing to its hierarchical composite structure, SiG as anode delivers the first discharge and charge capacity values as high as 3880 $mAhg^{-1}$ and 3016 $mAhg^{-1}$ respectively measured at the current rate of 205 mAg^{-1}. Even at high current rate (4.1 Ag^{-1}), SiG composite materials delivers first charge capacity of 1480 $mAhg^{-1}$ with good cycling performance (1040 $mAhg^{-1}$) after 1000 cycles. Due to its enhanced lithium storage, cycling stability and rate capability, synthesized SiG composites could be a potential anode candidate for Li-ion batteries.

* Corresponding author. Department of Chemistry, Vels Institute of Science, Technology and Advanced Studies (VISTAS), Chennai, 117, India.
E-mail address: a.m.shanmugharaj@gmail.com (A.M. Shanmugharaj).
[1] First author with equal contributions.

https://doi.org/10.1016/j.jpowsour.2019.227618
Received 4 September 2019; Received in revised form 16 November 2019; Accepted 12 December 2019
Available online 29 January 2020

1. Introduction

Innovative energy storage technologies are essentially important for the operation of electric vehicles and for the exploration on practical usage of many types of renewable energy sources [1–4]. Though the commercially available lithium battery technologies are favourable energy storage devices for portable electronics, they cannot meet requirements of advanced energy storage applications due to their confined energy storage capacity restricting its stable operation. Therefore, it is essentially important to develop alternative anode materials meeting the demands for energy storage requirements [5,6].

In recent eras, nanostructured silicon materials have received wide attention, not only for the many technological applications presently in use and envisioned for the future, but also from the research perspective on fundamental principles [6,7]. Owing to its overwhelming theoretical storage capacity (4200 $mAhg^{-1}$) in comparison to conventional carbonaceous materials (372 $mAhg^{-1}$) and reasonably low working potential (~0.5 V versus Li/Li^{+}), silicon is expected to be outstanding anode material for next generation lithium batteries for advanced energy storage applications [8–14]. Also, the elongated voltage plateau upon discharging enables a stable voltage during electrochemical cycling [15]. Extensive research work has been carried out on the synthesis and application aspects of several various nanostructured silicon based materials, such as nanoparticles [8,9], nanowires [10,11], nanotubes [1,12] and thin films [13,14]. However, the silicon anode undergoes a huge volume change (upto 400%) during galvanostatic charge−discharge cycle, leading to the pulverization of the silicon particles, which in turn results in drastic capacity fade [16,17]. One of the plausible solutions to circumvent this problem is to prepare a carbon coated silicon composite materials that minimizes dimensional changes and thereby overcoming the pulverization issues of Li alloy electrodes during cycling [18–21].

Though extensive research has been reported on the synthesis and application aspects of various nanostructured silicon's, very little work has been done on the two dimensional (2D) silicon nanomaterial with sheet morphologies having nanometer level thickness and submicro- to micrometer level lateral dimensions [22–25]. These nanomaterials have been receiving undue attention in recent years, since they show unusual physical properties, which are the results of a quantum size effect associated to their ultrathin structure [22,23]. Theoretical modelling studies on monolayer silicon nanosheet with (111) honeycomb arrangement, revealed that these sheets preferably exists in a low-buckled morphology [26,27]. Several experimental studies have also revealed that chemical functionalization of the single-layered Si nanosheet yields stable structures with unique properties [23–25]. Owing to the large volume expansion and thereby rapid capacity decay, the use of silicon nanosheets in next generation Li-ion batteries still remains a challenging task, though, it showed better lithium storage properties, when compared to silicon nanoparticles [28,29]. One of the remedial measures to overcome this issue is to encapsulate silicon sheets between the graphene sheets.

Ever since its discovery, two dimensional graphene nanosheets has been broadly explored in various application areas such as electronics, catalysis, sensing and energy storage [30–37] Alternatively, these nanosheets have become promising nanoscale building blocks for the development of new composite materials, thanks to its unique nanostructure with excellent properties [38,39]. Due to good electronic and mechanical properties with tunable surface chemistry, these nanomaterials can be used as an ideal template in controlling the properties of the nanocomposite materials. Significant research has been done in recent years on the development of graphene based nanostructured electrode materials for lithium-ion batteries [40–42]. Recently, Kim et al. [43], reported the bulk synthesis of silicon nanosheets by magnesiothermic reduction of sand and its graphene based composites with significantly improved lithium storage properties.

Alternatively, in the present research, we introduced a novel concept where the siloxene nanosheets prepared via. Topochemical reaction from calcium silicide ($CaSi_2$) is effectively intercalated between the graphene sheets by tuning its surface chemistry leading to few- to multi-layered graphene-siloxene composites (SiG). Synthesized graphene-siloxene nanostructures have been extensively characterized using various tools and examined for its electrochemical characteristics by fabricating lithium-ion half-cell using lithium metal as counter and reference electrode.

2. Experimental section

2.1. Synthesis of siloxene nanosheets

Synthesis of layered siloxene ($Si_6H_6O_3$) was done by following the method described by Yamanaka et al. [44], 10 g of $CaSi_2$ (Sigma Aldrich Inc., South Korea) was added to 37% HCl (Sigma Aldrich Inc., South Korea) at −10 °C in the ice-cold bath and stirring was continued for 5 days. The obtained product was filtered and washed with 10% hydrofluoric acid (HF; Sigma Aldrich Inc., South Korea) followed by acetone and then dried under vacuum at 110 °C yielding approximately 7 g of yellow coloured siloxene nanosheets [25].

2.2. Hydrosilylation reaction of siloxene sheets

Hydrosilylation reaction on the surface of siloxene nanosheets was carried out using allylamine under inert atmosphere [45]. Typically, siloxene nanosheets (0.87 g, 0.5 mmol) was dispersed in toluene (100 mL) into which a solution of $H_2PtCl_6{\cdot}6H_2O$ (0.68 g, 0.1 mmol) was added dropwise, followed by allylamine (1.45 g, 25 mmol). The heterogeneous mixture was left under stirring condition for one day in inert medium and the solvent was removed by rotary evaporation to yield pale yellow coloured powder (1.2 g).

2.3. Synthesis of graphene oxide (GO)

Modified Hummer's method was employed for synthesizing GO from purified natural graphite (Sigma–Aldrich) [46,47]. Briefly, Natural graphite flakes (1 g) was mixed with 100 mL of concentrated sulfuric acid and subjected to sonication using a Branson digital sonicator (S450D, 500 W, 30% amplitude) for 30 min followed by the addition of sodium nitrate (1 g) in an ice cold condition. To this mixture, potassium permanganate (6 g) was slowly added under stirring condition for 2 h, and subsequently the temperature was raised to 35 °C in a water bath for another 30 min. To this mixture, 46 mL of hot water (~70 °C) was added dropwise and successively the temperature of the system was increased to 98 °C. Lastly, 140 mL of hot water (~70 °C) was added, followed by 20 mL of 30 wt% hydrogen peroxide (H_2O_2) solution to terminate the reaction [48].The obtained graphite oxide was suspended in water and subsequently purified by dialysis to remove residual salts and acids. The resulting GO was dried under vacuum (40 mmHg) overnight at 55 °C to produce GO powder.

2.4. Preparation of graphene-siloxene composite materials

In typical procedure, graphene oxide (0.5 g in 1 L of acetone) dispersant was mixed with amine functionalized siloxene nanosheets dispersant (0.5 g in 1 L of acetone) and the resulting mixture was subjected to sonication for 2 h at 40 °C. Then the suspended particles was separated by filtration and dried under vacuum at 60 °C to generate graphene-siloxene (SiG) composite materials. The prepared materials were calcined at 800 °C under inert argon atmosphere for 12 h to yield black coloured powder. For comparison purpose, reduce graphene oxide (RGO) without a siloxene nanosheet was prepared by calcining the GO at 800 °C under inert atmosphere for 12 h. Physically blended RGO-siloxene nanosheets (SiG blend) were also prepared by mixing the RGO and topochemically synthesized silicon nanosheets at a specific weight ratio.

2.5. Characterization of the layered composite materials

The spectroscopic characterization silicon and graphene-siloxene composites were done using a Fourier Transform Infrared spectrometer (Spectrum one, Perkin Elmer, USA) in transmission mode in the wavenumber range of 4000–400 cm^{-1} at a resolution of 0.4 cm^{-1}. Samples for FT-IR characterization were prepared by making potassium bromide (KBr) pellets using 0.1 mg of finely dispersed samples in 100 mg of KBr powder. X-ray photoelectron spectroscopy (XPS, K-Alpha, Thermoelectron, Thermofischer Inc., USA) was employed to corroborate the surface chemical composition and functional groups present on the synthesized graphene-siloxene composites. Structural characterization of the synthesized materials was also performed using Raman spectroscopy (RFS/100s, Bruker, Germany). Morphological characterization of the prepared samples was carried out on a JEOL JEM-2100F transmission electron microscope (TEM) and a LEO SUPRA 55 field-emission scanning electron microscope (FE-SEM) equipped with an energy dispersive X-ray analysis (Carl Zeiss EDAX, GENESIS 2000). The XRD analysis was carried out on a Mac Science X-ray diffractometer (M18XHF-SRA) using Cu K_α radiation (λ = 1.5412 Å). Thermogravimetric analysis (TGA) was performed using a thermogravimetric analyzer (TGA Q5000 IR, TA instruments, USA) operated at a heating rate of 10 °C/min at nitrogen atmosphere kept at the nitrogen flow rate of 50 mL/min.

2.6. Electrochemical characterization

The electrochemical performances of calcium silicide ($CaSi_2$) and graphene-siloxene composites (SiG) were determined by fabricating coin Li-ion (2032 type) half cells. Electrodes were prepared by slurry coating technique using the composition of 80 wt % active material, 10 wt % of super P (TIMCAL) as additional conductive agent and 10 wt % of poly (vinylidene difluoride) (PVDF) (Kureha KF100) as binder onto copper foil, which acts as the current collector. The slurry was made by grinding the above composition in the presence of N-methyl pyrrolidone (NMP) solvent using mortar for 15 min and subsequently coated onto the copper foil and dried in oven for 10 h at 120 °C. About 16 mm diameter electrodes were punched out from the dried electrodes after pressing the samples under a 7T load. The punched electrode was assembled into coin cell (2032 type) using 1 M solution of lithium hexaflouro phosphate ($LiPF_6$) (in ethylene carbonate (EC) and diethyl carbonate (DEC) solvent) electrolyte and metallic lithium foil as the counter and reference electrode. Galvanostatic charge and discharge measurements of the fabricated coin cells were done in the voltage range of 0.1–1.5 V vs. Li/Li^+ using Wonatech battery analyzer. Electrochemical impedance spectroscopic characterization of the fabricated Li-ion coin cells were carried out by applying sine wave with amplitude of 5.0 mV in the frequency range of 100 kHz to 0.01 Hz.in VersaSTAT 3 electrochemical work station.

3. Results and discussion

Fig. 1 (a) illustrates the synthesis scheme of the graphene-siloxene (SiG) few- to multi-layered composites using calcium silicide. Initially, amine functionalized siloxene nanosheet is synthesized in two steps. In the first step, H terminated siloxene with Si (111) layers have been synthesized using calcium silicide by the synthetic route suggested by Yamanaka et al., [44]. These Si (111) layers consists of two dimensional (2D) silicon nanosheets stacked in the form a graphite like crystal with the in-plane hexagonal sublattice constant coinciding Si (111) plane (a = 0.385 nm) in the diamond structure [49]. In the second step, the synthesized siloxene nanosheets is functionalized with propylamine using a platinum catalysed hydrosilylation reaction using allylamine producing stable colloidal dispersion of propylamine functionalized siloxene sheets (Si–NH_2). The obtained amine functionalized siloxene nanosheets is easily dispersible in solvents such as chloroform, acetone

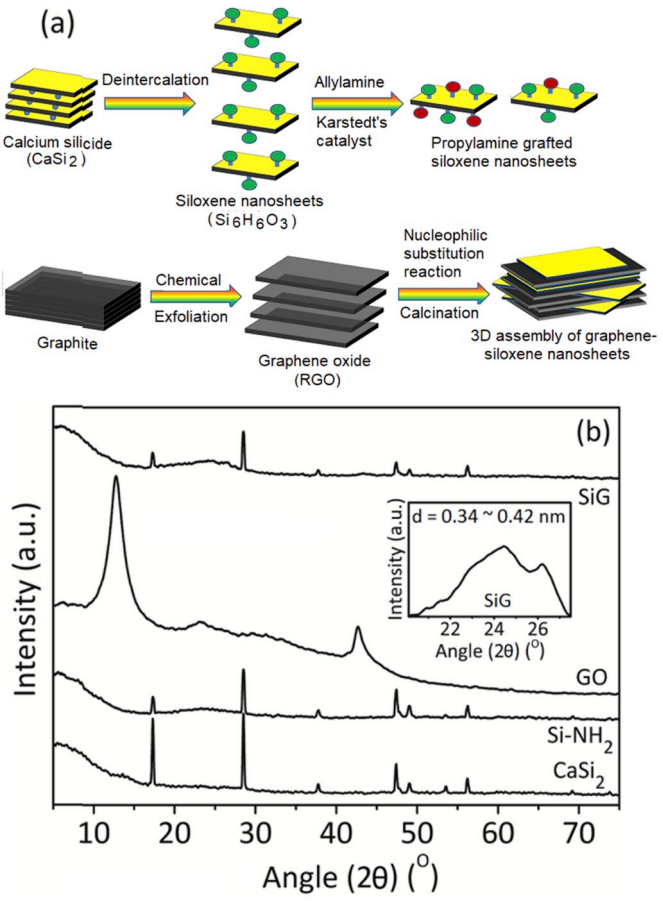

Fig. 1. (a) Schematic representation of silicon-graphene nanosheet based layered materials (b) X-ray diffraction results of calcium silicide ($CaSi_2$), Amine grafted silicon nanosheets (Si–NH_2), graphene oxide (GO) and silicon-graphene layered materials (SiG) (Inset: diffraction pattern of SiG in the selected 2θ range).

and ether, and insoluble in water and ethanol. The stable colloidal dispersion of siloxene nanosheets and graphene oxide (0.5 mg/mL) in acetone are mixed together and subjected to sonication for about 2 h at 40 °C. The resulting suspension is filtered, washed with acetone for several times and subsequently dried under vacuum to get black precipitate (SiG). Chemically prepared graphene oxide (GO) with epoxide groups on the basal plane undergoes nucleophilic substitution reactions with the grafted amine groups of siloxene sheets, resulting in the formation of graphene-siloxene composite materials (Fig. 1 (a)). Alternatively, -OH groups present on the GO surface reacts with the Si–OH groups of siloxene sheets leading to the surface grafted graphene-siloxene composites (Fig. 1 (a)).

To get more information on the crystallinity of SiG layered materials, XRD characterization were performed in the 2θ range of 5°~75° and the results are displayed in Fig. 1 (b). Pristine $CaSi_2$ showed several crystalline peaks at 2θ values of 17.2°, 28.7°, 37.7°, 47.4°, 48.9°, 53.5°, 56.1°, 69° and at 75°, which are attributed to the (003), (101), (104), (110), (311), (400) and (331) planes respectively (ICDD-JCPDS Card No. 75–2192) [50–52]. Alternatively, silicon nanosheets (SiH) produced by calcium de-intercalation process has the peaks at 2θ of 17.2°, 28.4°, 37.7°, 47.4°, 56.2° and at 69.3° along with a small peak at 12° that are corroborated to (110), (111), (104), (220), (311), (400), (331) and (001) crystal planes (ICDD-JCPDS Card No. 27–1402) (Fig. S1 (a & b), supporting information). The average d-spacing calculated using Bragg's equation for (001) crystal plane is observed to be 0.74 nm for SiH samples. Grafting of allylamine onto the siloxene sheets (Si–NH_2) doesn't lead to significant variations in the crystalline planes (110),

(111), (104), (220), (311), (400), (331) though there is a slight shift in (001) crystal plane to lower angle (2θ = 10.9°, Fig. S1 (c), supporting information) that correspond to the interlayer spacing of 0.81 nm. The crystalline domain sizes of the silicon nanosheets (SiH and Si–NH_2) were calculated using the well-known Scherrer's formula.

$$L_C = K\lambda/\beta cos\vartheta \quad (1)$$

where L_C is crystalline domain size in the C direction.

K is Scherrer's constant (0.89)
λ is X-ray wavelength (1.5412 Å)
β is angular width of diffracted peak at the half maximum (FWHM-Full Width Half Maximum) in radians for diffraction angle.
θ is the diffraction angle

The crystalline domain sizes are observed to be 11.3 nm (SiH) and 26.5 nm (Si–NH_2), which reveals the slight enhancement of L_C on grafting allylamine on its surface. As expected, pristine GO showed a strong peak at 2θ of 12.7° corresponding to the (001) interlayer d-spacing of 0.7 nm [48]. Alternatively, SiG layered materials showed the crystalline peaks corresponding to siloxene nanosheets along with two small peaks in the 2θ range of 21–24.5° (d-spacing, 0.36–0.42 nm) and at 26° (d-spacing, 0.34 nm) revealing the fact that GO exists in reduced state in this system. Broad peak with reduced peak intensity corresponding to (002) peak of graphitic carbon in SiG composite materials implies the existence of both exfoliated and few stacked layers of graphene sheets. For comparison purpose, XRD characterization of the thermally annealed graphene oxide (RGO) has also been done and the result is included in Fig. S1 (d). Complete disappearance of the (001) peak of GO with the appearance of broad peak in the 2θ range of 20–25° reveals the existence of both exfoliated and partially stacked layers of graphene sheets in RGO samples. There is no significant variation between RGO and SiG layered composite materials with respect to the (002) diffraction peak revealing the fact that the intercalation of siloxene nanosheets can expected to be present between the exfoliated graphene sheets in SiG materials. Since the thickness of single siloxene nanosheet is 0.28 nm [27], It is expected 1–2 layers of siloxene sheets are intercalated between the stacked graphene layers (with d spacing of 034–0.42 nm) in the multi-layered stacked arrangement of SiG layered materials. We didn't observe any distinct (001) crystalline diffraction peak of siloxene nanosheets in the synthesized SiG based layered materials and this fact may be attributed to the absence of multi-layered stacked arrangement of siloxene nanosheets as they are being intercalated within exfoliated/few layer stacked graphene sheets alongwith the presence of surface grafted siloxene nanosheets on graphene surface.

Fourier transform Infrared Spectroscopy (FT-IR) is used to identify and characterize the surface chemical interaction between graphene oxide and amine functionalized siloxene nanosheets (Fig. 2 (a)). Pristine $CaSi_2$ showed major peaks at 3451 (O–H stretching), 1629 (O–H bending), 1060 (Si–O–Si stretching), 800 cm^{-1} (Si–O–Si bending) apart from peak corresponding to 475 cm^{-1} (TO bands due to Si–Si crystal lattice vibration) revealing its oxidized nature [44,53]. Deintercalation of calcium ions resulted in the formation of layered siloxene ($Si_6H_6O_3$) and this fact is corroborated by the appearance of peaks at 2140 (Si–H stretching) and at 890 cm^{-1} (SiH_2 vibrations) along with the peaks at 3440 (OH stretching) and at 1080 cm^{-1} (Si–O stretching) (Fig. S1 (e), supporting information). Successful grafting of allylamine on siloxene nanosheets ($Si_6H_6O_3$) through hydrosilylation reaction is corroborated by the disappearance of Si–H peaks (2140 & 890 cm^{-1}) with the appearance of new peaks at 3400 (N–H stretching), 2920 (C–H stretching), 1621 (N–H bending), 1421 (C–H bending), 1250 (C–N stretching), 915 (C–N wagging) and 766 cm^{-1} (Si–C stretching) along with the peaks at 3480 (-OH stretching) and 1060 (Si–O–C stretching) (Fig. 2 (a)). Pristine GO synthesized by chemical exfoliation of graphite showed characteristic IR peaks at 1720 (C═O stretching), 1600 (skeletal

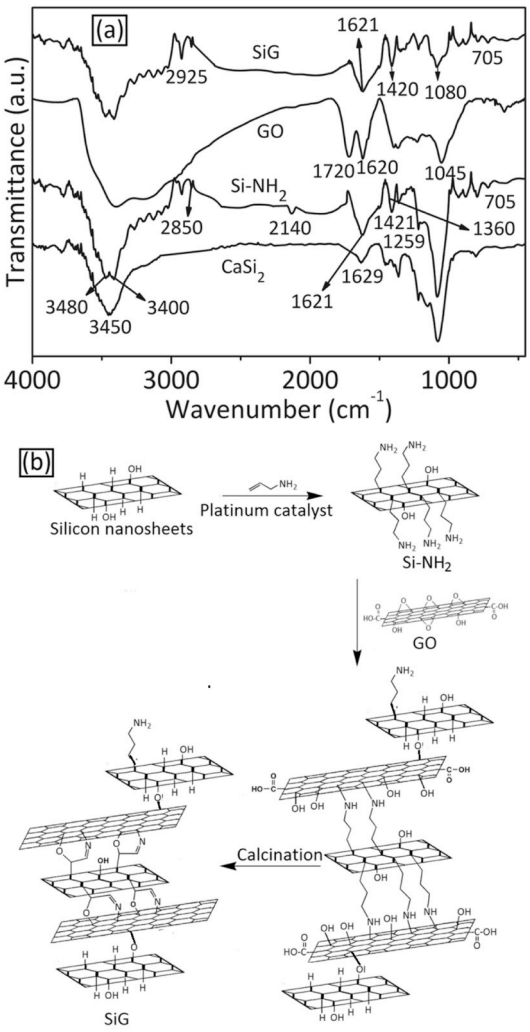

Fig. 2. (a) FT-IR spectra of $CaSi_2$, Si–NH_2, GO and SiG layered materials (b) Reaction mechanism between silicon nanosheets (SiH) and graphene oxide (GO).

vibrations of graphitic -C═C- domains), 1222 (C–OH stretching), 1045 (C–O stretching of epoxide group) [48,54,55]. Layered structure graphene-siloxene (SiG) composites showed characteristics IR absorption peaks at 2925 (C–H asymmetric stretching), 1602 (skeletal vibrations of graphitic -C═C- domains), 1421 (C–H bending vibrations), 1250 (C–N stretching), 915 (C–N wagging) and 766 (Si–C stretching) along with the broad peak at around 1080 cm^{-1} (C–O and Si–O stretching vibrations) corroborating successful formation of graphene-siloxene (SiG) layered materials. The possible mechanism of interaction between the graphene oxide and siloxene nanosheets before and after calcination is included in Fig. 2 (b).

To get more insights on the functional groups present in the SiG layered composite materials, XPS characterization was done and the results are displayed in Fig. 3 and Figs. S2 and S3 (supporting information). Survey scan results of the $CaSi_2$ showed strong peaks at 346 eV, 100.9 eV, and 531 eV representing Ca2p, Si2p and O1s peaks on this samples (Fig. S2 (a)). Deintercalation of calcium ions (Ca^{2+}) resulted in slight variation of peak intensities corresponding to Si2p (100 eV) and O1s (530.5 eV) peaks in siloxene nanosheets (SiH) (Fig. S2 (a)). Grafting of allylamine *via* hydrosilylation reaction resulted in the appearance of new peaks at 285 eV (C1s) and N1s (400 eV) along with the presence of Si2p (100 eV) and O1s (530.5 eV) peaks revealing the successful formation of propylamine grafted siloxene nanosheets (Si–NH_2) (Fig. S2 (a)). Survey scan results of GO showed peaks at 285 eV and 530 eV that

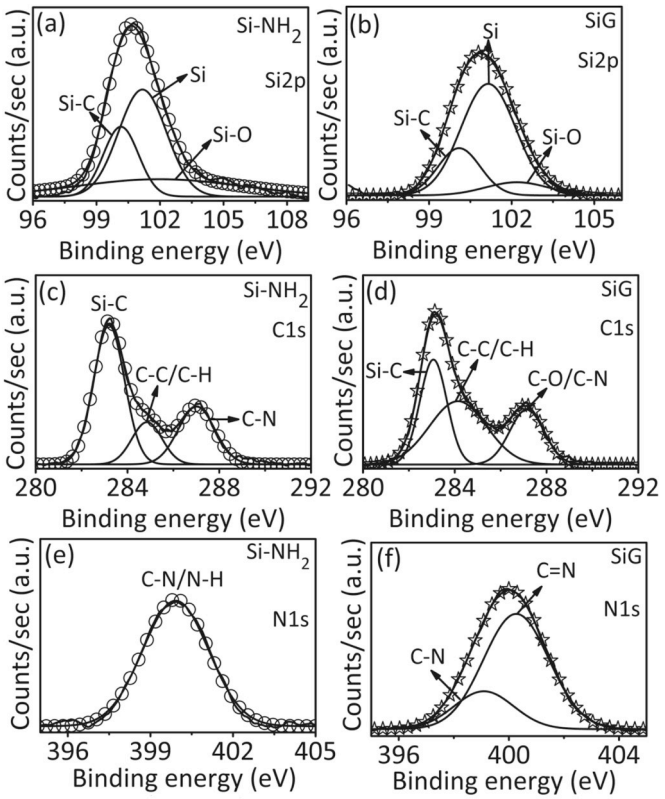

Fig. 3. High resolution Si2p (a, b), C1s (c, d) and N1s (e, f) results of Si–NH_2 and SiG layered materials.

are attributed to C1s and O1s peaks [54,55]. Alternatively, the presence of peaks corresponding to C1s (285 eV), O1s (530 eV) and Si2p (100 eV) clearly corroborates the formation of SiG composites (Fig. S2 (a)). To reveal the functional groups and nature of interaction between graphene and siloxene sheets in the synthesized SiG materials, deconvolution of high resolution spectra of C1s (285 eV), N1s (400 eV), Si2p (100 eV) and O1s (530 eV) were done and the results are displayed in Fig. 3 and Figs. S2 and S3 (supporting information).

Deconvolution of Si2p peaks of $CaSi_2$ showed two peaks, which corresponds to Si–Si (100.5 eV) and Si–O (102.6 eV) groups (Fig. S2 (b), supporting information). There is no significant variation in peak positions on deconvoluting Si2p peak of siloxene nanosheets (Si–Si, 101 eV; Si–O, 102.7 eV) (Fig. S2 (c), supporting information). However, drastic increase in peak intensity corresponding to Si–O (102.6 eV) group for SiH samples in comparison to $CaSi_2$ samples corroborates the introduction of oxygen functionalities during calcium deintercalation process. This fact is further confirmed by the rise in peak absorbance ratio of Si–O and Si–Si groups ($A_{Si\text{-}O}/A_{Si\text{-}Si}$, 0.07; $A_{Si\text{-}O}/A_{Si\text{-}Si}$, 0.36). The above interpretation is further supported by the appearance of single peak that corresponds to Si–O group (532.2 eV) in O1s high resolution spectra of $CaSi_2$ and SiH samples (Fig. S2 (c & d), supporting information). Formation of new peak at 99.9 eV (Si–C) along with the Si–Si (101.2) and Si–O (102.9 eV) peaks as evidenced from deconvoluted spectra of Si2p clearly corroborates the formation mechanism proposed in Fig. 2 (b). There is no significant variation in the Si2p deconvoluted peaks of SiG materials (Fig. 3 (b)), when compared to Si–NH_2 further supports our proposed mechanism as shown in Fig. 2 (b). To reveal the functional groups present between the siloxene and graphene interface, deconvolution of C1s spectra of Si–NH_2, GO and SiG materials was done and the results are displayed in Fig. 3 (b & c) and Fig. S3 (a), supporting information. Deconvolution of C1s spectra of Si–NH_2 showed three peaks corresponding to Si–C (283.5 eV; ~56.1%), C–C/C–H (284.8 eV; 16.6%) and C–N (286.8 eV; 27.4%). Similarly, deconvolution of C1s spectra of SiG also showed peaks at 283.3 (~34.1%), 284.6 (~43.3%) and 286.9 eV (~22.6%), which are attributed to Si–C, C–C/C–H and C–O/C–N groups. Significant rise in peak absorbance area ratio of C–C/C–H group of SiG (~43.3%) in comparison to Si–NH_2 (~16.6%) reveals the successful formation of graphene-siloxene layered materials. For comparison purpose, deconvolution of C1s spectra of GO was done and the results are displayed in Fig. S3 (a), supporting information. Deconvoluted C1s spectra of GO materials showed five peaks at 284.5, 285.6, 286.4, 287, 288 eV that are attributed to C–C/C–H, C–OH, C–O–C, C═O and –COO- groups [54,55]. In contrast to GO, significant reduction in oxygen functionalities is observed in SiG layered materials supporting our proposed mechanism (Fig. 2 (b)). The functional groups formed between the graphene and siloxene interface was further determined by deconvoluting N1s spectra of Si–NH_2 and SiG and the results are included in Fig. 3 (e & f). Deconvolution of N1s spectra of Si–NH_2 displayed one peak, which is correspond to C–N (399.7 eV) group (Fig. 3 (e)). In contrast, deconvoluted N1s spectra of SiG layered materials showed two peaks that are corroborated to C–N (399.2 eV) and C═N (400.3 eV) groups respectively (Fig. 3 (f)), further supporting our proposed mechanism as shown in Fig. 2 (b). Finally, deconvolution of O1s spectra was also done for Si–NH_2, GO and SiG to understand the oxygen functionalities in these materials and the results are included in Fig. S3 (b-d). While, the deconvoluted O1s spectra of GO showed peaks corresponding to O═C–OH (530.2 eV), C═O (531.5 eV) and C–O–C (532.4 eV) groups [54,55], O1s spectra of Si–NH_2 and SiG exhibit a single peak centered at 532.2 eV revealing the existence of C–O and Si–O groups in these materials.

The morphological features and elemental composition of synthesized SiG materials were characterized using Field emission scanning electron microscopy (FE-SEM) and the results are displayed in Fig. 4 and Fig. S4, supporting information. Pristine calcium silicide ($CaSi_2$) consists of several stacked layers of silicon sheets. Deintercalation of calcium ions followed by amine grafting resulted in sponge like with partially exfoliated siloxene nanosheets for Si–NH_2 samples (Fig. 4). As expected, graphene oxide (GO) nanosheets obtained from chemical exfoliated graphite consist of wrinkled morphologies (Fig. 4). Alternatively, intercalation and surface grafting of siloxene nanosheets on the graphene sheets is clearly corroborated using FE-SEM images, which form few- to multi-layered arrangement of nanosheets (Fig. 4 and Fig. S4). From the figure, it is clearly visible that few stacked sheets of siloxene present on the graphene sheets (yellow encircled regions) (Fig. S4 (a-c), supporting information). In contrast to few layered graphene-siloxene materials (Fig. S4 (a-d)), multi-layered SiG composite materials form bubbled structure on its surface due to the mismatch in the thermal expansion coefficient and trapped hydrocarbons between the siloxene and graphene sheets during calcination (Fig. 4 & Fig. S4 (d), supporting information) [56,57]. The size of bubbles formed on the SiG multi-layered materials are observed to be in the range of 50–200 nm.

To corroborate the presence of siloxene nanosheets in the graphene sheets, transmission electron microscopic characterization was done and the results are included in Fig. 4 and Fig. S5, supporting information. Pristine calcium silicide ($CaSi_2$) consists of several stacked layers of crystalline siloxene nanosheets with buckled morphology (Fig. S5 (a) supporting information). Deintercalation of calcium ions followed by amine grafting via hydrosilylation reaction results in the formation of amorphous few layered siloxene nanosheets (Fig. 4). Alternatively, grafting of graphene sheets via nucleophilic substitution reaction between amine grafted siloxene nanosheets and graphene oxide followed by calcination at 800 °C for desired time forms SiG composite materials with crystalline siloxene sheets intercalated between the graphene sheets (Fig. 4 and Fig. S5, supporting information, encircled regions). Earlier reports reveal that epoxide groups preferentially forms on the basal plane of graphene oxide (GO) during chemical exfoliation of graphite and hence, the intercalation of siloxene nanosheets within the graphene sheets is more feasible by our synthesis route. Appearance of carbon, silicon and oxygen peaks in energy dispersive analysis (EDX) as

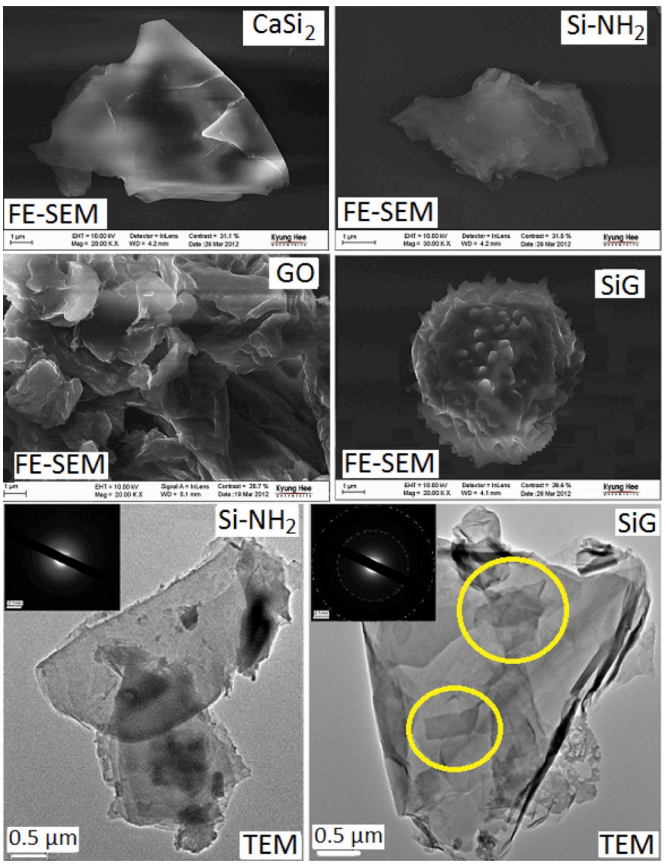

Fig. 4. FE-SEM results of $CaSi_2$, Si–NH_2, GO, SiG layered materials and TEM images of Si–NH_2, SiG layered materials.

well as X-ray mapping results showed the presence of siloxene in the graphene surface of the prepared SiG composite materials (Fig. S5, supporting information).

To obtain further understanding on the structural changes happened during the chemical processing from siloxene nanosheets (SiH) (derived from $CaSi_2$) to graphene-siloxene layered materials (SiG), Raman spectra were obtained and the results are included in Fig. S6 (a-d). The Raman spectrum of siloxene nanosheets (SiH) derived from topochemical reaction of $CaSi_2$ displays a small broad peak at around 508 cm^{-1} with a small hump at 450 cm^{-1} that are corroborated to E_{2g} vibrational mode (sp^3 hybridized state) of honeycomb structure of siloxene nanosheets and surface defect induced structural complexities in the siloxene nanosheets (Fig. S6 (a)) [58]. Grafting of allylamine on siloxene nanosheets (Si–NH_2) results in significant rise of peak intensity corresponding to the E_{2g} vibrational mode with a blue shift to higher wavenumber (~518 cm^{-1}) revealing its crystalline nature. Alternatively, two broad peaks centered at around 570 cm^{-1} and 475 cm^{-1} are observed for SiG nanosheet based layered materials. Significant blue shift of Raman peak to higher wavenumber (~570 cm^{-1}) corroborates that these siloxene nanosheets are under compressive stress (with sp^2 bond length) due to intercalation within the graphene sheets [58]. Another interesting observation that has been made in the present investigation is the formation of bubbled structures (50–200 nm) on the multi-layered graphene-siloxene nanosheet materials (SiG) due to the mismatch in thermal coefficient as well as degradation of trapped hydrocarbons during calcination (Fig. 4) [56,59].This fact is further confirmed from the Raman spectroscopic characterization of the synthesized SiG composite materials. Zabel et al., reported that biaxially strained graphene consisting of balloon or bubbled structures on its surface deposited on Si/SiO_X substrate results in the significant red shift of the peak corresponding to 2D' (~2700 cm^{-1}) and G (~1600 cm^{-1}) without drastic variation in D peak (~1350 cm^{-1}) [60]. Alternatively, Pan et al. [56], characterized the graphene/boron nitride heterostructures using Raman spectroscopy in which they observed shift in Raman peaks (G and 2D) on the bubbled surface. In the present work, we observed two G peaks at 1620 cm^{-1} (unstrained graphene) and at 1525 cm^{-1} (bubbled graphene) along with the appearance of broad D peak at 1350 cm^{-1} corroborating the presence of both unstrained and bubbled graphene structures in the synthesized SiG materials (Fig. S6 (b)). This fact is further revealed by the appearance of two 2D′ peaks (unstrained graphene, 2715 cm^{-1}; bubbled graphene, 2650 cm^{-1}) (Fig. S6 (c)).

To corroborate the nitrogen (N_2) surface area, pore size distribution and pore volume of the prepared SiG materials, Brunauer–Emmett–-Teller (BET) adsorption-desorption studies were done and the results are included in Fig. 5 and Table 1. For comparison purpose, BET surface area measurements for RGO and physically blended graphene-siloxene materials were also done and the results are displayed in Fig. 5 and Table 1. While all the characterized samples showed Type II adsorption-desorption patterns [61], the presence of hysteresis loop in these samples revealed the typical H3 type confirming the presence of non-rigid aggregates of plate like particles giving rise to slit shaped pores in these materials (Fig. 5). The nitrogen (N_2) surface area calculated using BET Nitrogen adsorption isotherm is significantly higher for SiG composite materials (Fig. 5), when compared to the GO (48.5 m^2g^{-1}, Fig. S8 (a)) or $CaSi_2$ (1.81 m^2g^{-1}) (Table 1). For comparison purpose, surface area of reduced graphene oxide (RGO and its blend with topochemically synthesized siloxene nanosheets (SiG-blend) were also done and the results are included in Table 1. It is noteworthy to mention that the surface area of SiG is observed to be 99%, 26% and 4.7% higher in comparison to $CaSi_2$, RGO and SiG-blend samples. Significantly higher surface area of SiG composite materials ensures fast lithium storage and also advantageous over volume change during lithium insertion-extraction process [61,62].The average pore volume determined using Barrett-Joyner-Halenda (BJH) method are observed to be 0.0067 cm^3g^{-1} ($CaSi_2$), 0.021 cm^3g^{-1} (GO), 0.136 cm^3g^{-1} (SiG-blend), 0.22 cm^3g^{-1} (RGO), 0.42 cm^3g^{-1} (SiG) respectively (Table 1). The remarkable improvement in pore volume for SiG materials relative to other materials implies that these layered materials will be more effective in accommodating the large volume variations during discharge-charge cycles. Also, significant variation in pore size distribution is noted for SiG materials, when compared to $CaSi_2$, RGO or SiG blend (Fig. 6). It is worthwhile to notice that $CaSi_2$ has intense pore volume (0.07 cm^3g^{-1}) with pore size ~2 nm revealing its microporous nature. However, relatively less intense pore volume peaks (0.02–0.03 cm^3g^{-1}) in the pore size range of 2–5 nm and a broad hump (pore

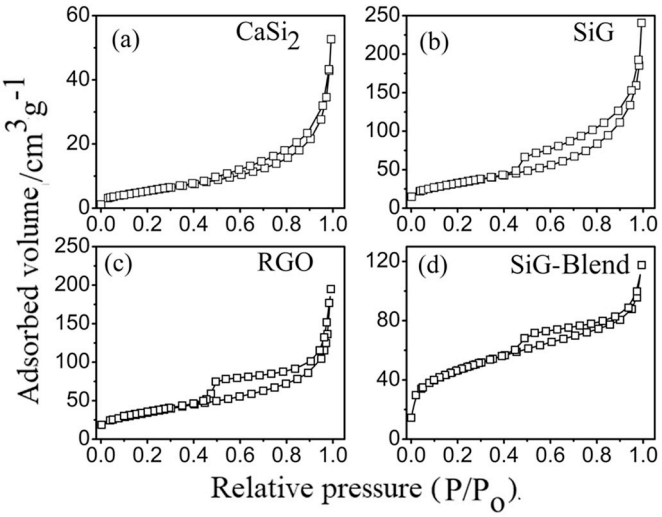

Fig. 5. BET results of (a) $CaSi_2$, (b) SiG, (c), RGO and (d) SiG-Blend materials.

Table 1
BET N_2 surface area results of $CaSi_2$ and SiG materials.

Samples	BET N_2 surface area (m^2/g)	Pore volume (cm^3g^{-1})
$CaSi_2$	1.81	0.0067
GO	48.5	0.021
SiG	168.5	0.42
RGO	117.5	0.22
SiG-blend	160.5	0.136

volume, 0.01 cm^3g^{-1}) in the range of 7–10 nm are corroborated to the mesoporous and macroporous structures present in the pristine $CaSi_2$. Similarly, the synthesized SiG materials also display sharp intense pore volume peak (0.7 cm^3g^{-1}) at ~2 nm and relatively less intense pore volume peaks (~0.4 cm^3g^{-1}) in the range 2–5 nm revealing its mesoporous structures. On contrary to $CaSi_2$, appearance of multiple pore volume peaks (0.05–0.1 cm^3g^{-1}) in the pore size range 5–12 nm revealed the formation of mesopores of varying sizes in SiG materials. Chemical grafting of siloxene on the graphene sheets induces macroporous structures due to the factors such as void formation (due to the degradation of hydrocarbons) and bubbling effect (due to mismatch in the thermal coefficient) as noticed in Raman spectroscopic results. To further elucidate the proposed theory, pore size distribution on GO, RGO and SiG blends were also done and the results are included in Fig. 6 and Fig. S7 (b). Interestingly, while GO exhibited higher pore population (pore volume, 0.01–0.02 cm^3g^{-1}) in the pore size ranging 1–50 nm corroborating its mesoporous and macroporous size (Fig. S7(b)), thermal reduction (RGO) resulted significant reduction in macroporous structures with the appearance of intense peaks (pore volume, 0.05–0.22 cm^3g^{-1}) in the pore size range of 1–5 nm revealing the existence of mesoporous structures (Fig. 6). Also, similar trend is noted for physical blended RGO and siloxene nanosheets (SiG-blend), which implies that the physical blending doesn't have substantial impact on the pore size distribution corroborating the fact that tuning the interface chemistry has considerable influence on the pore population.

Thermogravimetric analysis (TGA) was employed to determine the weight composition of the calcium silicide ($CaSi_2$), Si–NH_2, GO, RGO and SiG materials and the results are displayed in Fig. 7(a) and Fig. S8. Though 2 wt % loss is observed upto 285 °C for $CaSi_2$ samples, approximately 6 wt % gain has been noted in the temperature range of 285–800 °C due to the formation of Wollstanite ($CaSiO_3$) and siloxene dioxide (SiO_2) as shown in the reaction scheme 2 [63].

$$\mathbf{CaSi}_2 + 2.5\boldsymbol{O}_2 \rightarrow \boldsymbol{CaSiO}_3 + \boldsymbol{SiO}_2 \quad (2)$$

In contrast to $CaSi_2$, siloxene nanosheets (SiH) showed initial weight loss (~9 wt %) in the temperature range of 25–150 °C. However, 6% weight gain has been observed in this material on increasing the temperature range to 800 °C and this fact may be attributed to the oxidation of siloxene nanosheets (SiH) to SiO_2 (Fig. not shown). Alternatively, amine grafted siloxene nanosheets (Si–NH_2) exhibit a weight loss (~7 wt %) in the temperature range of 40–580 °C, which may be corroborated to the degradation of grafted propylamine formed on the siloxene nanosheets due to hydrosilylation reaction between siloxene nanosheets (SiH) and allylamine (Fig. 7(a)). In contrast to Si–NH_2, graphene-siloxene (SiG) nanosheet based layered materials showed approximately 3 wt % loss upto 300 °C with a major weight loss in the temperature range of 300–800 °C, which could be attributed to the degradation of graphene. For comparison, reduced graphene oxide (RGO) produced by calcination of GO was also done and the result is included in Fig. 7(a). In contrast to GO, which showed two degradation steps in the selected temperature range, reduced graphene oxide (RGO) showed a single degradation step and this fact may be attributed to the degradation of graphene in air environment (Fig. 7(a) and Fig. S8, supporting information). The residual weight of 59% in SiG composites materials is corroborated to the relative content of siloxene nanosheets in this system (Fig. 7(a)).

The electrochemical properties of the $CaSi_2$ and SiG as anodes in lithium-ion cells were evaluated *via* constant current charge/discharge cycling in the potential range of 0.01–2.0 V at the current rates of 205 mAg^{-1}, 410 mAg^{-1} and at 4100 mAg^{-1} (4.1 Ag^{-1}). The charge-discharge results at first five cycles of $CaSi_2$ and SiG based electrode measured at the current rate of 205 mAg^{-1} are included in Fig. S9 and Table S1. $CaSi_2$ based electrode showed two plateau's (~0.7 V and 0.15 V) delivering a first discharge capacity of 3372 $mAhg^{-1}$ (Fig. S10(a), Table S1). Appearance of two distinct plateaus is attributed to the alloy formation of lithium alloy with siloxene (Li_xSi) and calcium (Ca–Li). However, drastic drop in specific charge capacity (1319 $mAhg^{-1}$) is observed

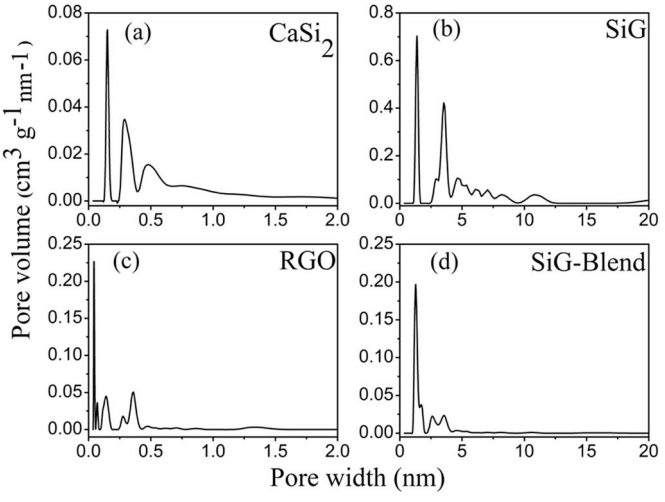

Fig. 6. Pore size distribution on (a) $CaSi_2$, (b) SiG, (c), RGO and (d) SiG-Blend materials.

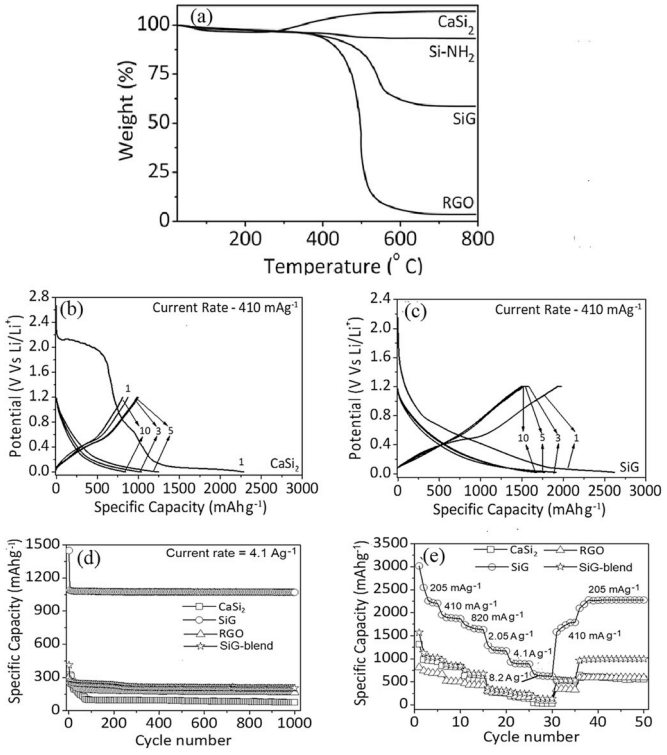

Fig. 7. (a)TGA results of $CaSi_2$, Si–NH_2, RGO and SiG layered materials, (b, c) Charge-discharge profiles of $CaSi_2$ and SiG, (d) Cycling performances of CaSi2, SiG, RGO and SiG-Blend at 4.1 Ag-1 current rates in 1000 cycles and (e) Electrochemical performances of CaSi2, SiG, RGO and SiG-Blend materials at various current rates.

during charging with the capacity retention of only 39%. In contrast, graphene-siloxene composite materials (SiG) exhibit a first discharge and charge capacities of 3880 $mAhg^{-1}$ and 3016 $mAhg^{-1}$ with the capacity retention of 78% (Fig. S9; Table S1). Higher Li storage capacity for the SiG nanosheet based layered materials in comparison to $CaSi_2$ is attributed to the synergistic contribution of graphene and siloxene in the lithium storage process. While the two dimensional siloxene nanosheets renders higher lithium storage capacity, the effective encapsulation of siloxene between the graphene sheets buffers the volume expansion and thereby maintains good capacity retention revealing the synergistic contribution of siloxene and graphene in the electrochemical performance. As indicated by the theoretical study, if all graphene nanosheets are strictly monolayer, the maximum lithium storage capacity of graphene is 744 mAh g^{-1}, corresponding to the formation of the Li_XC. Synthesized SiG contain 59 wt% of siloxene and therefore the theoretical capacity of SiG can be calculated as Total capacity = $C_{graphene}$ x 41% + C_{SiG} x 59%Where $C_{graphene}$ is the storage capacity of graphene and CSiG is the storage capacity of siloxene nanosheets (4200 mAh g^{-1}) [47].

$$\text{Total capacity} = 744 \text{ x } 0.41 + 4200 \text{ x } 0.59 = 2783 \text{ mAhg}^{-1}$$

The higher values of initial storage capacity of SiG layered materials are attributed to the additional storage of Li-ion in the nano-voids present in the graphene surface or micropores generated in the graphene surface during the oxidation-reduction process or nano-cavities generated due to the intercalated siloxene nanosheets in the graphene layers. To further validate our discussion, we have also carried out charge-discharge cycling behaviour of reduced graphene oxide (RGO) and physically blended graphene-siloxene (SiG blend) based electrodes at the current rate of 205 mAg^{-1} and the results are included in Fig. S9 (a). The first discharge and charge capacities of RGO and SiG-blend are noted to be 1250 (RGO), 920 (RGO), 2100 (SiG-blend) and 1510 $mAhg^{-1}$ (SiG-blend), respectively with the capacity retention values of 74% (RGO) and 72% (SiG-blend) revealing the fact that tuning the interface chemistry between siloxene and graphene has significant impact on the lithium-ion storage performance.

To evaluate the electrochemical reactions of the SiG nanosheet based layered materials during electrochemical cycling, the dQ/dV profiles were made by differentiating the first ten charge-discharge profiles and the results are displayed in Fig. S10. The main peak observed at around 0.07 V with an onset potential of ~0.12 V during the first discharge corresponding to the long flat plateau zone in the first discharge voltage profile is attributed to the phase transition of crystalline Si nanosheets to amorphous lithium silicide (Li_xSi). The strong peak at 0.47 V with a small peak at 0.38 V during the first charge could be ascribed to dealloying of the Li_XSi phase. Appearance of two peaks at 0.04 V, 0.09 V along with the broad hump at 0.21 V in the subsequent discharge cycles are corroborated to the phase transitions between amorphous Li_xSi, i.e., the phase transition from the P–I (LiSi) phase to the P-II (Li_7Si_3) phase and the subsequent transition to the P-III ($Li_{15}Si_4$) phase (0.09 V; broad hump at 0.21 V) and lithium intercalation in the graphene (0.04 V; LiC_X) [64].

Though, significant research reports has been published on one dimensional silicon nanowire based electrodes that showed excellent discharge and charge capacities, very little work has been done on the two dimensional (2D) silicon nanosheets as anode materials for lithium-ion batteries (Table S2). For instance, Yu et al. [29], reported first discharge and charge capacity values of 2553 $mAhg^{-1}$ and 1242 $mAhg^{-1}$ measured at the current rate 100 mAg^{-1} for siloxene nanosheets prepared by DC arc discharge (Table S2). Recently, Kim et al.,[43] reported first discharge and charge capacity of silicon nanosheet anode (discharge capacity, 3563 $mAhg^{-1}$; charge capacity, 2431 $mAhg^{-1}$) prepared by magnesium reduction of sand and its RGO based composites (discharge capacity, 3563 $mAhg^{-1}$; charge capacity, 2431 $mAhg^{-1}$) measured at the current rate of 200 mAg^{-1}. Alternatively, graphene-siloxene nanosheet based layered materials synthesized by tuning the interface chemistry has showed relatively better discharge (~9% increment) and charge capacities (~24% increment) at first cycle measured at the current rate of 205 mAg^{-1}, when compared to the RGO based silicon composites prepared from sand (Table S2). The relative decrement of the second discharge (~17%) and charge capacity (~15.6%) is observed to be lower for SiG composite materials in comparison to $CaSi_2$ based electrodes (discharge capacity, 54%; charge capacity, 25.4%). Both discharge and charge capacities remain nearly constant for subsequent cycles of SiG layered materials measured at the current rate of 205 mAg^{-1}, with little fading upto 5 cycles and these values are significantly higher when compared to $CaSi_2$ based electrodes (Table S1).

The charge-discharge profiles of $CaSi_2$, SiG, RGO and SiG-blend based anodes in the 1st, 3rd, 5th and 10th cycle measured at the current rate of 410 mAg^{-1} rate are shown in Fig. 7(b and c) and Fig. S9 (b&c). The first discharge and charge capacities of $CaSi_2$ are observed to be 2295 and 878 $mAhg^{-1}$, respectively with a first columbic efficiency of 61.7% (Fig. 7 (b)). Alternatively, the first discharge and charge capacities of SiG nanosheet based composite materials are observed to be 2618 and 1975 $mAhg^{-1}$, respectively with a coloumbic efficiency of 75.4% (Fig. 7 (c)). Contrastingly, the first discharge and charge capacities of RGO are observed 1210 $mAhg^{-1}$ and 790 $mAhg^{-1}$ with the capacity retention of 65.3% (Fig. S9). Similarly, the first discharge and charge capacities of SiG-blend are noted to be 2475 and 1050 $mAhg^{-1}$ with the capacity retention of only 42% (Fig. S9). After 3rd cycle, the discharge and charge capacities of SiG nanosheet based composite materials decreases to 1905 $mAhg^{-1}$ (discharge capacity) and 1590 $mAhg^{-1}$ (charge capacity) with the columbic efficiency of 83.5% (Fig. 7 (c)) and these values are significantly higher when compared to $CaSi_2$ (discharge capacity, 1245 $mAhg^{-1}$; charge capacity, 988 $mAhg^{-1}$; Coloumbic efficiency, 79.4%), RGO (discharge capacity, 600 $mAhg^{-1}$; charge capacity, 500 $mAhg^{-1}$; Coloumbic efficiency, 83%) and SiG-blend (discharge capacity, 875 $mAhg^{-1}$; charge capacity, 750 $mAhg^{-1}$; Coloumbic efficiency, 86%) based electrodes (Fig. S9). Similar trend is noticed at higher cycle number viz., 5th and 10th cycle revealing the enhanced electrochemical characteristics of the SiG material prepared by tuning the interface chemistry between the graphene and siloxene nanosheets. The galvanostatic charge-discharge studies of $CaSi_2$, SiG, RGO and SiG-blend based electrodes were done for 1000 cycles at the current rate of 4100 $mAhg^{-1}$ (4.1 Ahg^{-1}) and the results are included in Fig. 7(a and b). The initial charge capacities of SiG nanosheet based layered material at first cycle at the current rate 4.1 Ahg^{-1} is noted to be 1480 $mAhg^{-1}$ and this value is significantly higher, when compared to $CaSi_2$ (~380 $mAhg^{-1}$), RGO (300 $mAhg^{-1}$) and SiG-blend (450 $mAhg^{-1}$) based electrodes. The cyclability of all these electrodes were examined under long-term cycling over 1000 cycles at the current rates of 4100 $mAhg^{-1}$ (4.1 Ahg^{-1}), which demonstrated a good cyclic performance and reversibility (Fig. 7 (b)). After 1000 cycles, the SiG based electrodes still maintained a specific charge capacity as high as 1040 mAh g^{-1}, which represents a much enhanced performance than that of $CaSi_2$ (specific capacity, 100 mAh g^{-1}), RGO (specific capacity, 175 $mAhg^{-1}$) and SiG-blend (specific capacity, 250 $mAhg^{-1}$) based electrodes [34, 50].

Significantly higher reversible capacity of SiG nanosheet based layered materials in comparision to graphene or $CaSi_2$ is ascribed to the effective encapsulation of siloxene nanosheets between the graphene layers. The structural stress imposed during the Li^+ alloying/dealloying processes is effectively endured by the encapsulated siloxene nanosheets, preventing the volume change and thereby maintaining the relatively constant charge/discharge profiles, whereas the presence of siloxene nanosheets between the graphene layers prevents the aggregation of graphene layers leading to the enhanced lithium storage performance. In addition, the voids existing in graphene nanosheets can effectively buffer the volume expansion of 2D siloxene nanosheets, when reacting with lithium. Consequently, cracking and pulverization of the electrode can be avoided, resulting in an enhanced cycling stability. To

validate the enhanced electrochemical performances of SiG based anode materials, FE-SEM characterization of the SiG electrode surface was done and the results are included in Fig. S11. Relatively rough surface with packed arrangement of multi-layered SiG composite materials is corroborated from the morphological results of the before cycled SiG electrode (Fig. S11 (a-c)). After 1000 cycles, electrode surface retains its morphological features with the appearance of minor cracks on the surface corroborating the formation of solid electrolyte interface (SEI) layer with controlled volume expansion of SiG materials (Fig. S11 (d-f)).

The specific charge capacities of $CaSi_2$ and SiG based anode materials at various current rates were also determined and the results are shown in Fig. 7 (e). As expected the specific capacity decreases with increasing current rates in all samples. However, the decrement in specific capacity with increasing current rates is less for SiG based composite materials in comparison to $CaSi_2$, RGO and SiG-blend based electrodes (Fig. 7 (e)). For instance, the first specific charge capacity of SiG electrode decreased to 1975 $mAhg^{-1}$ (410 mAg^{-1}), 1738 $mAhg^{-1}$ (820 mAg^{-1}), 1291 $mAhg^{-1}$ (2.05 Ag^{-1}), 975 $mAhg^{-1}$ (4.1 Ag^{-1}), 720 $mAhg^{-1}$ (8.2 Ag^{-1}) from 3016 $mAhg^{-1}$ (205 mAg^{-1}). Alternatively, the first specific charge capacity of $CaSi_2$ based electrodes decreased to 865 $mAhg^{-1}$ (410 mAg^{-1}), 640 $mAhg^{-1}$ (820 mAg^{-1}), 320 $mAhg^{-1}$ (2.05 Ag^{-1}), 201 $mAhg^{-1}$ (4.1 Ag^{-1}), 63 $mAhg^{-1}$ (8.2 Ag^{-1}) from 1318 $mAhg^{-1}$ (205 mAg^{-1}) (Fig. 7 (e)). Similarly, the first specific charge capacity of RGO based electrodes decreased to 650 $mAhg^{-1}$ (410 $mAhg^{-1}$), 460 $mAhg^{-1}$ (820 $mAhg^{-1}$), 286 $mAhg^{-1}$ (2.05 Ag^{-1}), 195 $mAhg^{-1}$ (4.1 Ag^{-1}), 135 $mAhg^{-1}$ (8.2 Ag^{-1}) from 847 $mAhg^{-1}$ (205 mAg^{-1}). Likewise, the first specific charge capacity of SiG-blend based electrodes decreased to 970 $mAhg^{-1}$ (410 $mAhg^{-1}$), 745 $mAhg^{-1}$ (820 $mAhg^{-1}$), 399 $mAhg^{-1}$ (2.05 Ag^{-1}), 256 $mAhg^{-1}$ (4.1 Ag^{-1}), 185 $mAhg^{-1}$ (8.2 Ag^{-1}) from 1570 $mAhg^{-1}$ (205 mAg^{-1}). Significantly higher capacity values of SiG based electrodes corroborating its enhanced electrochemical performance in comparison to $CaSi_2$, RGO and SiG-blend based electrodes. Moreover, when the current rate returns to 410 mAg^{-1} after 35th cycle, SiG based electrodes recovers its 61% (1570 $mAhg^{-1}$) of its initial specific capacity values, whereas, only 43% ($CaSi_2$), 39% (RGO) and 36% (SiG-blend) recovered in other electrode systems. Furthermore, on returning the current rate to 205 mAg^{-1}, SiG based electrodes recovered to 2275 $mAhg^{-1}$ (76% of its initial specific capacity) after 50th cycle and this value is significantly higher, when compared to $CaSi_2$, RGO and SiG-blend based electrodes that have recovered only 560 $mAhg^{-1}$ (42% of its initial specific capacity), 590 $mAhg^{-1}$ (70% of its initial specific capacity) and 970 $mAhg^{-1}$ (62% of its initial specific capacity) after 50th cycle corroborating good reversibility and excellent cyclability of SiG based electrodes.

To get more understandings on the outstanding electrochemical properties, electrochemical impedance spectroscopy (EIS) of $CaSi_2$, RGO, SiG-blend and SiG nanosheet based composite materials was carried in the frequency range of 100 kHz–0.01 Hz to confirm the interfacial electrochemistry and reaction mechanism. The typical Nyquist plots of AC impedance measured before and after cycling of all electrode systems are shown in Fig. 8 (a & b). Generally, the impedance spectrum consists of depressed arc followed by the straight line inclined at 45° angle and the equivalent circuit adopted for EIS calculation is shown in Fig. S12. While, the internal ohmic resistance, involving the resistance of the electrolyte and other resistive components, corresponding to the intercept of the plots with the real axis (Z_{re}) at high frequency is represented as R_e, the R_f and C_{dl1} values corresponding to the semicircle at high frequency region is demonstrated as resistance (R_f) and capacitance (C_{dl1}) of solid electrolyte-interface (SEI) films. On the contrary, R_{ct} and C_{dl2} values related to the semicircle at medium-to-low frequency are correlated to the charge transfer resistance (R_{ct}) and capacitance (C_{dl2}) and the Warburg impedance noted as Z_W referring the sloping region at low frequency is directly correlated to the lithium-ion diffusion process in the electrode. The values of R_e, R_f, R_{ct} and R_{total} are listed in Table 2.

R_e, which represents the internal resistance of the fabricated cell, is slightly lower before and after cycling for SiG based electrodes in comparison to the other electrode systems. R_{sf}, which corresponds to the SEI film resistance is significantly lower for SiG based electrodes (51.2 Ω), when compared to the $CaSi_2$ (293.4 Ω), RGO (169.3 Ω) and SiG-blend based electrodes (296.1 Ω). This result corroborates the fact that the effective encapsulation of siloxene nanosheets between the graphene sheets by tuning the interface chemistry (SiG) can buffer the volume effect of siloxene nanosheets and also inhibits the growth of passive layer on siloxene nanosheets. Significant reduction in R_{sf} value after 50th electrochemical cycling for all electrode systems reveals the ease of Li^+ ion diffusion (Table 2). R_{ct} values that provide information on charge-transfer resistance decreased significantly for SiG electrode (78.3 Ω) corroborating its lower charge transfer resistance in comparison to $CaSi_2$ (713.8 Ω), RGO (634.4 Ω) and SiG-blend (1097.2 Ω) based electrodes. As expected, significant reduction in charge-transfer resistance is observed after 50th electrochemical cycling for all electrode systems revealing the enhanced electrical conductivity in these systems. Similar trend is observed in R_{total} values before and after cycling revealing faster electrode kinetics in SiG electrodes, when compared to pristine $CaSi_2$, RGO and SiG-blend based electrodes (Table 2). This fact is further confirmed from the exchange current density (i_0) that has been calculated using the equation $i_0 = RT/nFR_{ct}$, where R is the gas constant, T is the absolute temperature, n is the number of electrons, F is the Faraday constant and R_{ct} is the charge-transfer resistance [33,40,59]. Relatively, higher value of exchange current density (i_0) for SiG ($33x10^{-5}$ Å) based electrodes in comparison to other electrode systems ($CaSi_2$, $3.6x10^{-5}$ Å; RGO, $4.1x10^{-5}$ Å and SiG-blend, $2.4x10^{-5}$ Å), implying enhanced electrochemical activity in the former (SiG electrodes). Interestingly, exchange current density (i_0) increases significantly for all electrode systems ($CaSi_2$, ~300%; RGO, ~235%; SiG-blend, ~550% and SiG, ~84%) corroborating significant rise in electrochemical activity after 50th cycles.

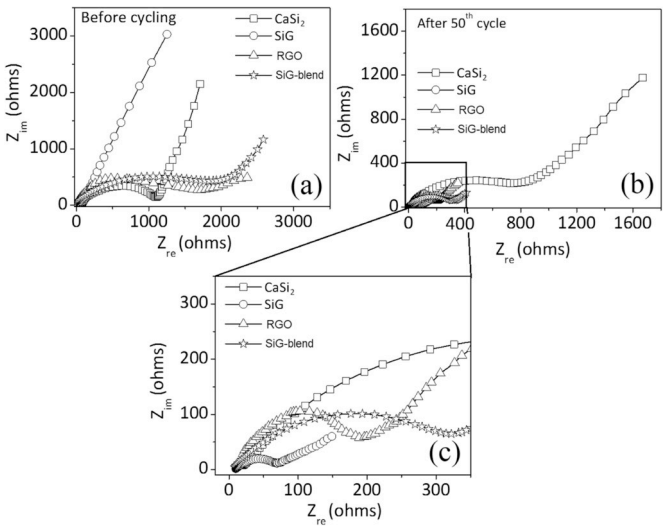

Fig. 8. (a, b) EIS results of CaSi2, SiG, RGO and SiG-Blend before and after cycling, (c) Expanded view at high frequency range.

4. Conclusions

In summary, graphene-siloxene (SiG) nanosheet based few- to multi-layered composite materials have been successfully synthesized by tuning the interface chemistry of graphene oxide and siloxene nanosheets followed by calcination at 800 °C. Successful formation of layered SiG materials is revealed using FE-SEM results. Effective encapsulation of crystalline siloxene nanosheets within graphene sheets is corroborated using TEM. Crystalline characteristics of encapsulated siloxene nanosheets are further confirmed using X-ray diffraction patterns. Significant rise in surface area for SiG layered materials in comparison to

Table 2
EIS results of calcium silicide ($CaSi_2$) and silicon-graphene (SiG) based electrodes before and after cycling.

Resistances	Before cycling				After cycling			
	$CaSi_2$	SiG	RGO	SiG-blend	$CaSi_2$	SiG	RGO	SiG-blend
R_S (Ω)	10.7	8.2	24.3	26.6	30.3	9.35	32.6	26.4
R_f (Ω)	293.4	51.2	169.3	296.1	72.4	13.0	24.4	39.4
R_{ct} (Ω)	713.8	78.3	634.4	1097.2	179.6	42.5	189.6	169.2
R_{total} (Ω)	1017.9	137.7	828.0	1130.0	282.3	64.8	246.7	235.0
I_A ($^x10^{-5}$ Å)	3.6	33.0	4.1	2.36	14.4	60.8	13.6	15.3

calcium silicide ($CaSi_2$) is further elucidated using the BET nitrogen adsorption-desorption studies. Galvanostatic charge-discharge studies of SiG based anode materials, when measured at the current rate of 205 mAg^{-1}, displayed the first discharge and charge capacities of 3880 $mAhg^{-1}$ and 3030 $mAhg^{-1}$ respectively. Similarly, at the current rate of 410 mAg^{-1}, the SiG based anode materials exhibit first discharge and charge capacities of 2618 $mAhg^{-1}$ and 1975 $mAhg^{-1}$. Even at very high current rate (4.1 Ag^{-1}), the prepared SiG based anode materials showed excellent reversible capacity of 1040 $mAhg^{-1}$ after 1000 electrochemical cycles. The overwhelming electrochemical properties of the prepared SiG is attributed to the synergistic effects of the unique combination of properties, which include outstanding electric conductivity due to the graphene, effective lithium-ion transport and controlled volume change due to encapsulation of siloxene nanosheets within the graphene sheets. These results demonstrate that SiG based layered materials could be promising anode materials for practical lithium ion battery applications. We strongly believe that our synthetic route could be extended to the development of high-performance anode materials for rechargeable batteries.

Author contributions

A.M.S generated the research idea, proposed the research plan, interpreted the data and wrote the manuscript. K.T, M.J.K.R and G.S carried out material characterizations as per the research plan proposed by A.M.S. K.T & M.J.K.R fabricated the Li-ion batteries, compiled the experimental results and helped in data interpretation and manuscript preparation. S.R, R.K and S.R provided research support for this project, helped in data analysis and manuscript preparation.

Acknowledgements

We grateful acknowledges the financial support from the Department of Science and Technology, Government of India ((DST/ECR/SERB/000815/2017), New Delhi. The **first author (K. Thileep Kumar)** is grateful to the financial support from the DST, Grant Junior Research fellow (JRF).

Appendix A. Supplementary data

Supplementary data to this article can be found online at https://doi.org/10.1016/j.jpowsour.2019.227618.

References

[1] J.M. Tarascon, M. Armand, Issues and challenges facing rechargeable lithium batteries, in: Materials for Sustainable Energy: A Collection of Peer-Reviewed Research and Review Articles. Nat, 2011, pp. 171–179, https://doi.org/10.1142/9789814317665_0024.
[2] K. Kang, Y.S. Meng, J. Bréger, C.P. Grey, G. Ceder, Electrodes with high power and high capacity for rechargeable lithium batteries, Sci 311 (2006) 977–980, https://doi.org/10.1126/science.1122152.
[3] K.T. Nam, D.W. Kim, P.J. Yoo, C.Y. Chiang, N. Meethong, P.T. Hammond, Y. M. Chiang, A.M. Belcher, Virus-enabled synthesis and assembly of nanowires for lithium ion battery electrodes, Sci 312 (2006) 885–888, https://doi.org/10.1126/science.1122716.
[4] M.S. Balogun, H. Yang, Y. Luo, W. Qui, Y. Huang, Z.Q. Liu, Y. Tang, Achieving high gravimetric energy density for flexible lithium-ion batteries facilitated by core-double-shell electrodes, Energy Environ. Sci. 11 (2018) 1859–1869, https://doi.org/10.1039/C8EE00522B.
[5] G. Diao, M.S. Balogun, S.Y. Tang, X. Guo, X. Huang, Y. Mao, Y. Tang, Low-valence bicomponent $(FeO)_X(MnO)_{1-X}$ nanocrystals embedded in amorphous carbon as high-performance anode materials for lithium storage, J. Mater. Chem. 6 (2018) 15274–15283, https://doi.org/10.1039/C8TA05015E.
[6] M.S. Balogun, W. Qiu, J. Jian, Y. Huang, Y. Luo, H. Yang, C. Liang, X. Lu, Y. Tong, Vanadium nitride nanowire supported SnS_2 nanosheets with high reversible capacity as anode material for lithium-ion batteries, ACS Appl. Mater. Interfaces 7 (2015) 23205–23215, https://doi.org/10.1021/acsami.5b07044.
[7] F. Priolo, T. Gregorkiewicz, M. Galli, T.F. Krauss, Silicon nanostructures for photonics and photovoltaics, Nat. Nanotechnol. 9 (2014) 19–24, https://doi.org/10.1038/nnano.2013.271.
[8] X.H. Liu, L. Zhong, S. Huang, S.X. Mao, T. Zhu, J.Y. Huang, Size-dependent fracture of silicon nanoparticles during lithiation, ACS Nano 6 (2012) 1522–1531, https://doi.org/10.1021/nn204476h.
[9] Y.M. Lin, K.C. Klavetter, P.R. Abel, N.C. Davy, J.L. Snider, A. Heller, C.B. Mullins, High performance silicon nanoparticle anode in fluoroethylene carbonate-based electrolyte for Li-ion batteries, Chem. Commun. 48 (2012) 7268–7270, https://doi.org/10.1039/C2CC31712E.
[10] C.K. Chan, H. Peng, G. Liu, K. McIlwrath, X.F. Zhang, R.A. Huggins, Y. Cui, High-performance lithium battery anodes using silicon nanowires, Nat. Nanotechnol. 3 (2008) 31–35, https://doi.org/10.1038/nnano.2007.411.
[11] M.R. Zamfir, H.T. Nguyen, E. Moyen, Y.H. Lee, D. Pribat, Silicon nanowires for Li-based battery anodes: a review, J. Mater. Chem. A. 1 (2013) 9566–9586, https://doi.org/10.1039/C3TA11714F.
[12] Z. Wen, G. Lu, S. Mao, H. Kim, S. Cui, K. Yu, X. Huang, P.T. Hurley, O. Mao, J. Chen, Silicon nanotube anode for lithium-ion batteries, Electrochem. Commun. 29 (2013) 67–70, https://doi.org/10.1016/j.elecom.2013.01.015.
[13] M.S. Balogun, W. Qiu, Y. Luo, H. Meng, W. Mei, A. Onasanya, T.K. Olaniyi, A review of the development of full cell lithium-ion batteries: the impact of nanostructured materials, Nano Res. 9 (2016) 2823–2851, https://doi.org/10.1007/s12274-016-1171-1.
[14] C. Yu, X. Li, T. Ma, J. Rong, R. Zhang, J. Shaffer, Y. An, Q. Liu, B. Wei, H. Jiang, Silicon thin films as anodes for high-performance lithium-ion batteries with effective stress relaxation, Adv. Energy Mater. 2 (2012) 68–73, https://doi.org/10.1002/aenm.201100634.
[15] J.R. Szczech, S. Jin, Nanostructured silicon for high capacity lithium battery anodes, Energy Environ. Sci. 4 (2011) 56–72, https://doi.org/10.1039/C0EE00281J.
[16] R.A. Huggins, Lithium alloy negative electrodes, J. Power Sources 81 (1999) 13–19, https://doi.org/10.1016/S0378-7753(99)00124-X.
[17] L.Y. Beaulieu, K.W. Eberman, R.L. Turner, L.J. Krause, J.R. Dahn, Colossal reversible volume changes in lithium alloys, Electrochem. Solid State Lett. 4 (2001) A137–A140, https://doi.org/10.1149/1.1388178.
[18] S.H. Ng, J. Wang, D. Wexler, K. Konstantinov, Z.P. Guo, H.K. Liu, Highly reversible lithium storage in spheroidal carbon-coated silicon nanocomposites as anodes for lithium-ion batteries, Angew. Chem. Int. Ed. 45 (2006) 6896–6899, https://doi.org/10.1002/anie.200601676.
[19] N. Liu, Z. Lu, J. Zhao, M.T. McDowell, H.W. Lee, W. Zhao, Y.A. Cui, Pomegranate-inspired nanoscale design for large-volume-change lithium battery anodes, Nat. Nanotechnol. 9 (2014) 187, https://doi.org/10.1038/nnano.2014.6.
[20] J.G. Ren, C. Wang, Q.H. Wu, X. Liu, Y. Yang, L. He, W.A. Zhang, Silicon nanowire–reduced graphene oxide composite as a high-performance lithium ion battery anode material, Nanoscale 6 (2014) 3353–3360, https://doi.org/10.1039/C3NR05093A.
[21] M. Ge, J. Rong, X. Fang, C. Zhou, Porous doped silicon nanowires for lithium ion battery anode with long cycle life, Nano Lett. 12 (2012) 2318–2323, https://doi.org/10.1021/nl300206e.
[22] U. Kim, I. Kim, Y. Park, K.Y. Lee, S.Y. Yim, J.G. Park, H.G. Ahn, S.H. Park, H. J. Choi, Synthesis of Si nanosheets by a chemical vapor deposition process and their blue emissions, ACS Nano 5 (2011) 2176–2181, https://doi.org/10.1021/nn103385p.
[23] Y. Sugiyama, H. Okamoto, T. Mitsuoka, T. Morikawa, K. Nakanishi, T. Ohta, H. Nakano, Synthesis and optical properties of monolayer organosilicon nanosheets, J. Am. Chem. Soc. 132 (2010) 5946–5947, https://doi.org/10.1021/ja100919d.
[24] H. Nakano, T. Mitsuoka, M. Harada, K. Horibuchi, H. Nozaki, N. Takahashi, T. Nonaka, Y. Seno, H. Nakamura, Soft synthesis of single-crystal silicon monolayer sheets, Angew. Chem. Int. Ed. 45 (2006) 6303–6306, https://doi.org/10.1002/anie.200600321.

[25] H. Okamoto, Y. Kumai, Y. Sugiyama, T. Mitsuoka, K. Nakanishi, T. Ohta, H. Nozaki, S. Yamaguchi, S. Shirai, H. Nakano, Silicon nanosheets and their self-assembled regular stacking structure, J. Am. Chem. Soc. 132 (2010) 2710–2718, https://doi.org/10.1021/ja908827z.

[26] E.C. Anota, A.B. Hernández, M. Castro, G.H. Cocoletzi, Investigating the electronic properties of silicon nanosheets by first-principles calculations, J. Mol. Model. 18 (2012) 2147–2152, https://doi.org/10.1007/s00894-011-1235-9.

[27] M.J. Spencer, T. Morishita, I.K. Snook, Reconstruction and electronic properties of silicon nanosheets as a function of thickness, Nanoscale 4 (2012) 2906–2913, https://doi.org/10.1039/C2NR30100H.

[28] Z. Lu, J. Zhu, D. Sim, W. Zhou, W. Shi, H.H. Hng, Q. Yan, Synthesis of ultrathin silicon nanosheets by using graphene oxide as template, Chem. Mater. 23 (2011) 5293–5295, https://doi.org/10.1021/cm202891p.

[29] X. Yu, F. Xue, H. Huang, C. Liu, J. Yu, Y. Sun, X. Dong, G. Cao, Y. Jung, Synthesis and electrochemical properties of silicon nanosheets by DC arc discharge for lithium-ion batteries, Nanoscale 6 (2014) 6860–6865, https://doi.org/10.1039/C3NR06418B.

[30] K.S. Novoselov, A.K. Geim, S.V. Morozov, D. Jiang, Y. Zhang, S.V. Dubonos, I. V. Grigorieva, A.A. Firsov, Electric field effect in atomically thin carbon films, Sci 306 (2004) 666–669, https://doi.org/10.1126/science.1102896.

[31] D. Wang, R. Kou, D. Choi, Z. Yang, Z. Nie, J. Li, L.V. Saraf, D. Hu, J. Zhang, G. L. Graff, J. Liu, Ternary self-assembly of ordered metal oxide− graphene nanocomposites for electrochemical energy storage, ACS Nano 43 (2010) 1587–1595, https://doi.org/10.1021/nn901819n.

[32] J. Xiao, D. Mei, X. Li, W. Xu, D. Wang, G.L. Graff, W.D. Bennett, Z. Nie, L.V. Saraf, I. A. Aksay, J. Liu, Hierarchically porous graphene as a lithium–air battery electrode, Nano Lett. 11 (2011) 5071–5078, https://doi.org/10.1021/nl203332e.

[33] A.M. Shanmugharaj, W.S. Choi, C.W. Lee, S.H. Ryu, Electrochemical performances of graphene nanosheets prepared through microwave radiation, J. Power Sources 23 (2011) 10249–10253, https://doi.org/10.1016/j.jpowsour.2011.08.039.

[34] Y. Li, H. Wang, L. Xie, Y. Liang, G. Hong, H. Dai, MoS_2 nanoparticles grown on graphene: an advanced catalyst for the hydrogen evolution reaction, J. Am. Chem. Soc. 133 (2011) 7296–7299, https://doi.org/10.1021/ja201269b.

[35] Y. Liang, Y. Li, H. Wang, J. Zhou, J. Wang, T. Regier, H. Dai, Co_3O_4 nanocrystals on graphene as a synergistic catalyst for oxygen reduction reaction, Nat. Mater. 10 (2011) 780–786, https://doi.org/10.1038/nmat3087.

[36] F. Schedin, A.K. Geim, S.V. Morozov, E.W. Hill, P. Blake, M.I. Katsnelson, K. S. Novoselov, Detection of individual gas molecules adsorbed on graphene, Nat. Mater. 6 (2007) 652–655, https://doi.org/10.1038/nmat1967.

[37] Y. Wang, Z. Li, D. Hu, C.T. Lin, J. Li, Y. Lin, Aptamer/graphene oxide nanocomplex for in situ molecular probing in living cells, J. Am. Chem. Soc. 132 (2010) 9274–9276, https://doi.org/10.1021/ja103169v.

[38] F. Schedin, A.K. Geim, S.V. Morozov, E.W. Hill, P. Blake, M.I. Katsnelson, K. S. Novoselov, Detection of individual gas molecules adsorbed on graphene, Nat. Mater. 6 (2007) 652, https://doi.org/10.1038/nmat1967.

[39] Y. Wang, Z. Li, D. Hu, C.T. Lin, J. Li, Y. Lin, Aptamer/graphene oxide nanocomplex for in situ molecular probing in living cells, J. Am. Chem. Soc. 132 (2010) 9274–9276, https://doi.org/10.1021/ja103169v.

[40] D. Li, M.B. Müller, S. Gilje, R.B. Kaner, G.G. Wallace, Processable aqueous dispersions of graphene nanosheets, Nat. Nanotechnol. 3 (2008) 101–105, https://doi.org/10.1038/nnano.2007.451.

[41] Y. Gan, L. Sun, F. Banhart, One-and two-dimensional diffusion of metal atoms in graphene, Small 4 (2008) 587–591, https://doi.org/10.1002/smll.200700929.

[42] A.M. Shanmugharaj, S.H. Ryu, Excellent electrochemical performance of graphene-silver nanoparticle hybrids prepared using a microwave spark assistance process, Electrochim. Acta 74 (2012) 207–214, https://doi.org/10.1016/j.electacta.2012.04.057.

[43] R. Liu, J. Duay, S.B. Lee, Heterogeneous nanostructured electrode materials for electrochemical energy storage, Chem. Commun. 47 (2011) 1384–1404, https://doi.org/10.1039/C0CC03158E.

[44] R. Raccichini, A. Varzi, S. Passerini, B. Scrosati, The role of graphene for electrochemical energy storage, Nat. Mater. 14 (2015) 271–279, https://doi.org/10.1038/nmat4170.

[45] W.S. Kim, Y. Hwa, J.H. Shin, M. Yang, H.J. Sohn, S.H. Hong, Scalable synthesis of silicon nanosheets from sand as an anode for Li-ion batteries, Nanoscale 6 (2014) 4297–4302, https://doi.org/10.1039/C3NR05354G.

[46] S. Yamanaka, H. Matsu-ura, M. Ishikawa, New deintercalation reaction of calcium from calcium disilicide. Synthesis of layered polysilane, Mater. Res. Bull. 31 (1996) 307–316, https://doi.org/10.1016/0025-5408(95)00195-6.

[47] H. Nakano, M. Nakano, K. Nakanishi, D. Tanaka, Y. Sugiyama, T. Ikuno, T. Ohta, Preparation of alkyl-modified silicon nanosheets by hydrosilylation of layered polysilane (Si_6H_6), J. Am. Chem. Soc. 134 (2012) 5452–5455, https://doi.org/10.1021/ja212086n.

[48] W.S. Hummers Jr., R.E. Offeman, Preparation of graphitic oxide, J. Am. Chem. Soc. 80 (1958), https://doi.org/10.1021/ja01539a017, 1339-1339.

[49] N.I. Kovtyukhova, P.J. Ollivier, B.R. Martin, T.E. Mallouk, S.A. Chizhik, E. V. Buzaneva, A.D. Gorchinskiy, Layer-by-layer assembly of ultrathin composite films from micron-sized graphite oxide sheets and polycations, Chem. Mater. 11 (1999) 771–778, https://doi.org/10.1021/cm981085u.

[50] A.M. Shanmugharaj, J.H. Yoon, W.J. Yang, S.H. Ryu, Synthesis, characterization, and surface wettability properties of amine functionalized graphene oxide films with varying amine chain lengths, J. Colloid Interface Sci. 401 (2013) 148–154, https://doi.org/10.1016/j.jcis.2013.02.054.

[51] J.R. Dahn, B.M. Way, E. Fuller, J.S. Tse, Structure of siloxene and layered polysilane (Si_6H_6), Phys. Rev. B. 48 (1993) 17872, https://doi.org/10.1103/PhysRevB.48.17872.

[52] K. Xu, L. Ben, H. Li, X. Huang, Silicon-based nanosheets synthesized by a topochemical reaction for use as anodes for lithium ion batteries, Nano Res. 8 (2015) 2654–2662, https://doi.org/10.1007/s12274-015-0772-4.

[53] D. Amalric-Popescu, F. Bozon-Verduraz, Infrared studies on SnO_2 and Pd/SnO_2, Catal. Today 70 (2001) 139–154, https://doi.org/10.1016/S0920-5861(01)00414-X.

[54] H. Okamoto, Y. Sugiyama, H. Nakano, Synthesis and modification of silicon nanosheets and other silicon nanomaterials, Chem. A Eur. J. 17 (2011) 9864–9887, https://doi.org/10.1002/chem.201100641.

[55] W. Wang, E. Xie, N. Jiang, D. He, Ion beam synthesis and characterization of yttrium silicide, Appl. Surf. Sci. 199 (2002) 1–5, https://doi.org/10.1016/S0169-4332(01)00577-3.

[56] S.H. Ryu, A.M. Shanmugharaj, Influence of long-chain alkylamine-modified graphene oxide on the crystallization, mechanical and electrical properties of isotactic polypropylene nanocomposites, Chem. Eng. J. 422 (2014) 552–560, https://doi.org/10.1016/j.cej.2014.01.101.

[57] S.H. Ryu, A.M. Shanmugharaj, Influence of hexamethylene diamine functionalized graphene oxide on the melt crystallization and properties of polypropylene nanocomposites, Mater. Chem. Phys. 146 (2014) 478–486, https://doi.org/10.1016/j.matchemphys.2014.03.056.

[58] A.S. Mayorov, R.V. Gorbachev, S.V. Morozov, L. Britnell, R. Jalil, L. A. Ponomarenko, A.K. Geim, Micrometer-scale ballistic transport in encapsulated graphene at room temperature, Nano Lett. 11 (2011) 2396–2399, https://doi.org/10.1021/nl200758b.

[59] E. Cinquanta, E. Scalise, D. Chiappe, C. Grazianetti, B. Van den Broek, M. Houssa, A. Molle, Getting through the nature of silicene: an sp^2–sp^3 two-dimensional silicon nanosheet, J. Phys. Chem. C 117 (2013) 16719–16724.

[60] J. Zabel, R.R. Nair, A. Ott, T. Georgiou, A.K. Geim, K.S. Novoselov, C. Casiraghi, Raman spectroscopy of graphene and bilayer under biaxial strain: bubbles and balloons, Nano Lett. 12 (2012) 617–621, https://doi.org/10.1021/nl203359n.

[61] X.H. Liu, L. Zhong, S. Huang, S.X. Mao, T. Zhu, J.Y. Huang, Size-dependent fracture of silicon nanoparticles during lithiation, ACS Nano 6 (2012) 1522–1531, https://doi.org/10.1021/nn204476h.

[62] A.Y. Khodakov, W. Chu, P. Fongarland, Advances in the development of novel cobalt Fischer− Tropsch catalysts for synthesis of long-chain hydrocarbons and clean fuels, Chem. Rev. 107 (2007) 1692–1744, https://doi.org/10.1021/cr050972v.

[63] Y. Cui, Z. Wen, Y. Liu, A free-standing-type design for cathodes of rechargeable Li–O_2 batteries, Energy Environ. Sci. 4 (2011) 4727–4734, https://doi.org/10.1039/C1EE02365A.

[64] F.J. Sotomayor, K.A. Cychosz, M. Thommes, Characterization of micro/mesoporous materials by physisorption: concepts and case studies, Acc. Mater. Surf. Res. 3 (2018) 34–50.